Title

Small, Clickable, and Monovalent Magnetofluorescent Nanoparticles Enable Mechanogenetic Regulation of Receptors in a Crowded Live-Cell Microenvironment

Journal

Nano Letters, 19(6)

ISSN

1530-6984

Authors

Kwak, Minsuk
Gu, Wonji
Jeong, Heekyung
et al.

Publication Date

2019-06-12

DOI

10.1021/acs.nanolett.9b00891

Peer reviewed

HHS Public Access

Author manuscript

Nano Lett. Author manuscript; available in PMC 2020 June 12.

Published in final edited form as:

Nano Lett. 2019 June 12; 19(6): 3761–3769. doi:10.1021/acs.nanolett.9b00891.

Small, clickable, and monovalent magnetofluorescent nanoparticles (MFNs) enable mechanogenetic regulation of receptors in a crowded live cell microenvironment

Minsuk Kwak[1,2,3,4,#], **Wonji Gu**[6,7,#], **Heekyung Jeong**[6,7,8], **Hyunjung Lee**[1,2,3], **Jung-uk Lee**[6,7,8], **Minji An**[6,7], **Yong Ho Kim**[4,5], **Jae-Hyun Lee**[6,7], **Jinwoo Cheon**[6,7,8,†], and **Young-wook Jun**[1,2,3,6,7,†]

[1]Department of Otolaryngology, University of California, San Francisco, San Francisco, California, USA.

[2]Department of Pharmaceutical Chemistry, University of California, San Francisco, San Francisco, California, USA.

[3]Helen Diller Family Comprehensive Cancer Center (HDFCCC), University of California, San Francisco, San Francisco, California, USA.

[4]SKKU Advanced Institute of Nanotechnology (SAINT), SKKU, Suwon, Republic of Korea

[5]Department of Chemistry, SKKU, Suwon, Republic of Korea

[6]Center for Nanomedicine, Institute for Basic Science (IBS), Seoul, Republic of Korea.

[7]Yonsei-IBS Institute, Yonsei University, Seoul, Republic of Korea.

[8]Department of Chemistry, Yonsei University, Seoul, Republic of Korea.

Abstract

Multifunctional magnetic nanoparticles have shown great promises as next-generation imaging and perturbation probes for deciphering molecular and cellular processes. As a consequence of multicomponent integration into a single nanosystem, pre-existing nanoprobes are typically large and show limited access to biological targets present in a crowded microenvironment. Here, we apply organic-phase surface PEGylation, click chemistry, and charge-based valency discrimination principles to develop compact, modular, and monovalent magnetofluorescent nanoparticles

[†]Correspondence should be addressed to J.C. (jcheon@yonsei.ac.kr) or Y.J. (young-wook.jun@ucsf.edu).

Author Contributions

M.K., and W.G. contributed equally. M.K., W.G., J.C., and Y.J. conceived and designed the project; M.K., W.G., and H.L. designed and performed the biological experiments; M.K., W.G., H.J., J.L., M.A., J.H.L., and Y.J. contributed to nanoparticle synthesis; M.K., W.G., H.J., and J.L. performed experiments and analyzed the data; Y.K. and J.H.L. provided the reagents and insightful discussions; M.K., J.C., and Y.J. wrote the manuscript; All authors discussed and commented on the manuscript.

[#]These authors contributed equally.

Supporting Information

The Supporting Information is available free of charge on the ACS Publication website at DOI:

» Oligonucleotide sequences, optical microscopy, synthesis of zinc-doped iron oxide ($Zn_{0.4}Fe_{2.6}O_4$) nanoparticles, silica-coating of $Zn_{0.4}Fe_{2.6}O_4$, organic-phase PEGylation of silica-coated $Zn_{0.4}Fe_{2.6}O_4$ (M@SiO_2), aqueous synthesis of PEGylated M@SiO_2, amine quantification, monovalent DNA conjugation of PEGylated M@SiO_2, synthesis of monovalent MPNs, DBCO-fluorescent dye conjugation of nanoparticles, plasmid constructions, Cell Line Generations, micro-magnetic tweezer set-up, live cell mechanogenetics experiment, immunostaining and flow cytometry, image processing and statistical analysis

» 15 supplementary Figures (Fig. S1 – Fig. S15)

(MFNs). We show that MFNs exhibit highly efficient labeling to target receptors present in cells with a dense and thick glycocalyx layer. We use these MFNs to interrogate E-cadherin-mediated adherens junction formation and F-actin polymerization in 3D space, demonstrating the utility as modular and versatile mechanogenetic probes in the most demanding single-cell perturbation applications.

Keywords

Magnetic nanoparticles; single cell perturbation biology; cell labeling; steric crowding; cell surface microenvironment

Single-cell perturbation tools, as epitomized by optogenetics, have provided an unprecedented means of interrogating the mechanisms underlying complex cell signaling processes[1,2]. These tools enabled selective and specific control of cellular activities including channel gating and biomolecular clustering, scaffolding, and dissociation with high spatiotemporal resolution[3,4]. Strategies using nanomaterials such as nanopatterns[5–8], biopolymers[9], DNA nanostructures[10–12], and nanoparticles[13,14] have been proposed recently toward developing alternative and complement single cell perturbation tools. Comparable characteristic lengths (e.g. size, assembly spacing) of these nanomaterials with those of cell signaling biomolecules ideally suit for labeling[15–17] and regulating spatial dynamics of targeted receptors[18–23]. These materials can also serve as nanoscale transducers that convert many different forms of physical inputs (e.g. optical, magnetic, and electronic stimulations) into biologically translatable cues[24–27]. Hence, these features of nanomaterials have enabled applications of single cell perturbation biology into diverse biological targets, which have been difficult with traditional tools.

As an example of such nanotechnology-driven single cell perturbation tools, we recently developed a mechanogenetic (*i.e.* genetically encoded mechanical control of cell signaling) tool using monovalent and modular magnetoplasmonic nanoparticles (MPNs)[28,29]. We further demonstrated its utility to identify the differential roles of spatial and mechanical cues in two important mechanosensitive receptors: Notch and vascular endothelial cadherin (VE-cadherin). While both receptor studies were successful, we observed that MPNs exhibited significantly reduced labeling to VE-cadherin than to Notch. In fact, cell surface receptors are present in a ‘sterically crowded’ microenvironment composed of bulky membrane receptors as well as glycoproteins and glycans, which form the complex polymer meshwork called glycocalyx[30,31]. Since bulky proteins and glycocalyx form a dense layer at the proximal cell surface and contribute to an overall negative charge[32], we hypothesized that VE-cadherin (approximately 15-nm tall)[33] is less accessible than Notch (approximately 100-nm tall in an extended form)[34] to MPNs due to the steric constraints. Considering that most animal epithelial cells form a thick glycocalyx layer, a decreased labeling of MPNs to small receptors limits broad applications of mechanogenetics.

A simple and straightforward solution to this problem is the development of a smaller nanoparticle probe enhancing diffusion through a sterically crowded microenvironment, while maintaining the capacity of MPNs to image and manipulate targeted cell surface receptors. Unfortunately, fabrication of monovalent MPNs smaller than 40 nm is

synthetically challenging due to incomplete gold shell formation. Even with the potential synthetic success, size reduction of MPNs can be a problem that leads to significantly decreased probe imaging signals, indistinguishable from background scattering signals from cellular components (e.g. endosomes). Use of a smaller magnetic core weakens force-generating capability of MPNs.

To address this challenge, as an alternative mechanogenetic probe with improved usability, applicability, and versatility, here we present small, clickable, and monovalent magnetofluorescent nanoparticle (MFNs). We first describe design and synthesis of MFNs and their monovalent conjugation with a targeting oligonucleotide. We investigate the performance of MFNs with respect to labeling efficiency, target specificity, and mechanogenetic control of receptors through flow cytometry, confocal microscopy, and magnetic tweezing in live cells. We show that the MFN significantly outperforms its predecessor, MPN, finally enabling mechanogenetic interrogation of epithelial cadherin (E-cadherin) surrounded by a highly crowded microenvironment.

The key components that comprise the mechanogenetic nanoparticle probes are 1) a force-generating domain that delivers a controlled mechanical force to the target protein, 2) an imaging domain that reports spatiotemporal distribution of the probes, and 3) a targeting domain that specifically binds to the receptor. The previously developed MPNs integrate all three components, where $Zn_{0.4}Fe_{2.6}O_4$ magnetic core (13 nm) coated with a thin (2 nm) SiO_2 layer ($M@SiO_2$), a plasmonic Au shell (thickness: > 10 nm), and an oligonucleotide tether serve as the force-generating, imaging, and targeting domains, respectively[29]. The gold shell additionally facilitates 1) formation of a robust, dense, and thin polyethylene glycol (PEG) surface passivation layer providing excellent colloidal nanoparticle stability[35,36], 2) modular conjugation with the targeting domain via well-established Au-S chemistry[37], and thereby 3) isolation of monovalent MPNs under harsh purification conditions. Since the gold shell comprises a significant portion of MPNs, its replacement with a smaller component while keeping other components can significantly reduce the total probe size. Hence, we sought to develop a method to directly conjugate surface ligands to $M@SiO_2$ nanoparticles, while providing the functions of the gold shell. Our strategy toward this design is to integrate organic-phase PEGylation, click chemistry, and a charge-based valency discrimination principle (Fig. 1a). The organic-phase PEGylation of nanoparticles minimizes undesired side reactions (e.g. hydrolysis of ester electrophiles), promotes complete PEGylation of surface amine functional group, and finally forms a dense passivation layer on the nanoparticle surface (Fig. 1a). Click chemistry facilitates modular and controlled functionalization of nanoparticles with imaging and targeting molecules[38,39]. The charge-based valency discrimination principle enables purification of monovalent nanoparticles through anion exchange high-performance liquid chromatography (AE-HPLC).

The surface PEGylation was carried out by reacting amine-functionalized $M@SiO_2$ with tetrafluorophenyl (TFP)-ester functionalized PEG molecules in anhydrous dimethylsulfoxide (DMSO) solution. Briefly, 100 pmol of amine-functionalized nanoparticles in 250 μL anhydrous DMSO were mixed with 20.8 μmol of TFP-$(OCH_2CH_2)_{24}$-X (X = OCH_3 or N_3; OCH_3:N_3 = 25:1) and 30 μmol of trimethylamine (Fig. S1). After overnight incubation, 50

μmol of succinic anhydride and 50 μmol of triethylamine dissolved in 50 μL anhydrous DMSO were added to quench residual amine functional groups. The resulting solution was then passed through a magnetic column with deionized water eluent, yielding stable aqueous dispersion of PEGylated nanoparticles. To form a dense but thin PEG passivation layer, we chose a short PEG molecule bearing 24 ethylene glycol (EG) repeats rather than traditional high molecular weight PEGs (e.g. PEG 5000). To determine the amine-to-PEG conversion efficiency, we quantified the number of amine functional groups per nanoparticle before and after the PEGylation. We observed semi-quantitative conversion of amine-functional groups to PEG_{24} ligands (> 94%), forming a dense PEG passivation layer with a surface density of 3.7 PEG_{24} per nm^2 (Fig. 1b). Accordingly, the resulting nanoparticles are colloidally stable with a hydrodynamic size of 29 nm, significantly smaller than an MPN (56 nm) (Fig. 1c; Fig. S1). Contrarily, a conventional aqueous-phase PEGylation resulted in poor passivation (1.9 PEG_{24} per nm^2) and particle aggregation (Fig. 1b,c).

The azide end-functional group of the PEG ligands allows for facile and modular click conjugation of this compact magnetic nanoparticle with any desired functional components such as fluorescent molecules, nucleic acids, or proteins. Using this, we first introduced a targeting module to the nanoparticles by reacting them with 5'-dibenzylcyclooctyne (DBCO)-modified oligonucleotides. To confirm the DNA conjugation, we loaded as-synthesized samples into an AE-HPLC column and compared the elution profiles with negative controls (*i.e.* nanoparticles without DNA or with amine-modified DNA). A broad peak was consistently seen at 8.5 min for all three samples, corresponding unconjugated bare particles. In contrast, additional three resolvable peaks around 13–15 minutes were seen only from the nanoparticles reacted with DBCO-DNA, indicating specific DNA-nanoparticle conjugation via click chemistry (Fig. 1d). Since the charge density of DNA-conjugated nanoparticles increases as a function of DNA valency (*i.e.* charge-based valency discrimination), we interpreted these peaks as mono-, di-, and multi (3 or more)-valent species[29,40]. The reactions with 30x excess DBCO-DNA produced significantly more monovalent nanoparticles (35.0%) than those with 10x DNA (13.9%), indicating the nanoparticle valency is controllable by varying the stoichiometric ratio (Fig. S2, Fig. S3). We only collected monovalent species for downstream applications, to ensure one-to-one probe-target engagement and minimize non-specific probe perturbation. We validated the monovalency of the particles by reacting them with ten-fold molar excess amount of monovalent gold nanoparticles (10 nm) bearing sequences complementary with the DBCO-DNA[37,41]. We observed the formation of a new single band by gel electrophoresis in between magnetic and gold nanoparticle bands (Fig. 1e)[42,43]. This band consisted nearly exclusively of $M@SiO_2$-Au heterodimers as revealed by transmission electron microscopy (TEM) (94%, Fig. 1f), strongly supporting monovalent DNA conjugation of the magnetic nanoparticles.

Next, we introduced the fluorescence-imaging module to the monovalent magnetic nanoparticles by click conjugation with DBCO-functionalized fluorescent dyes (AlexaFluor 647 or AF647). Gel electrophoresis confirmed the conjugation (Fig. 1g), finally forming monovalent magnetofluorescent nanoparticles (here and after MFNs) (Fig. 1h). The total internal reflection fluorescence (TIRF) images showed bright single-particle fluorescence signals with reasonably high photostability over multiple rounds of acquisition (Fig. 1g, Fig.

S4a,b). The single MFN exhibited approximately 30 times brighter signals than a single dye (Fig. S4c–e). Coupling of fluorescent components to magnetic nanoparticles has been previously reported[44–46], but our study is the first demonstration of monovalent MFNs bearing a single targeting moiety.

With the monovalent MFNs synthesized, we then tested our initial hypothesis: The compact nanoparticles would facilitate access to cell surface receptors in a crowded microenvironment, would improve the target labeling, and hence would allow mechanogenetic interrogation of cell surface receptors that have been difficult with MPNs (Fig. 2a). To test this hypothesis, we generated a U2OS cell line co-expressing a recombinant human Notch1 fused with SNAP- and mCherry-tags at its N and C termini (SNAP-hN1-mC), respectively, and a recombinant human E-cadherin fused with Halo- and GFP tags at its N and C termini (Halo-Ecad-GFP), respectively. Homogenous cell surface expression of these receptors was confirmed by treating the cells with cell-impermeable dyes (e.g. SNAP surface or Halo-ligand dyes) (Fig. S5). We chose the Notch and Cadherin co-expression system, because 1) overexpression of large and highly glycosylated Notch receptors form a dense and thick glycocalyx layer at the cell surface and 2) E-cadherin is a relatively small protein. Hence, nanoparticle targeting to E-cadherin would be hindered by Notch overexpression. This co-expression system further allows a direct comparison of the probe labeling to a tall and a short protein in same cells. The Notch or E-cadherin receptors were targeted by nanoparticles (MFNs or MPNs) via benzylguanine (BG)-SNAP tag or chloroalkane-Halo tag chemistries, respectively.

We first compared targeting capabilities of MPNs and MFNs to Notch. To make MPNs compatible with cytometry analysis (Fig. S6), we introduced DBCO-AF647 dyes to MPNs. Cells treated with MPNs exhibited a peak shift in the AF647 channel to a higher fluorescence compared to negative control cells, indicating an increased nanoparticle labeling. Cells treated with MFNs in identical conditions exhibited a slightly more shifted peak (Fig. 2b). To compare the labeling efficiency of the MPN-treated cells with the MFN-treated cells, we calculated the geometric means of AF647 intensity and then normalized the values per single particle (*i.e.* MPN or MFN) fluorescence signals (Fig. S7). Labeling with MFNs showed more increases in nanoparticle fluorescence signal (2.06 fold) than labeling with MPNs (1.53 folds) (Fig. 2c). This result shows that both MPNs and MFNs label tall and easily accessible receptors efficiently and specifically (*i.e.* Notch), where MFNs showed a slightly better labeling.

Improved labeling capacity of MFNs over MPNs is more evident, when targeted to E-cadherin present in a sterically crowded environment. We observed cells treated with MPN labeling exhibited a negligible peak shift in the AF647 channel with very small increase (1.08 folds) in average fluorescence intensity, compared to the negative control. In an identical labeling condition, cells treated with MFNs showed a significant 647 nm peak shift in the channel with a 6.0-fold increase in the mean fluorescence intensity (Fig. 2b,c). Increasing MFN concentration (5 nM) provided further improvement, as indicated by the mean fluorescence intensity (23-fold increase) and the frequency of cells with dense nanoprobe labeling (44.4%) (Fig. 2b–d). To examine the effect of receptor variance (*i.e.* Notch vs. E-cadherin) in the nanoparticle labeling, we also generated cells expressing

SNAP-tagged Notch receptors with the EGF repeat truncation (ΔEGF-Notch) (Fig. S8). This Notch variant has a comparable size (approximately 10 nm) with E-cadherin and keeps spatial and signaling dynamics of full-length Notch[47–49]. Consistent to the E-cadherin case, only MFNs showed robust labeling to the cells expressing ΔEGF-Notch, while MPNs exhibited negligible receptor labeling (Fig 2b,c, and Fig. S8). This result supports our notion that environmental steric crowding of target receptors and the nanoparticle size are major determinants of the cell labeling.

We analyzed the specificity to target receptors of MFN probes. Based on GFP signals, we determined the gate that classified the analyzed cells into two groups; one containing cells with high E-cadherin expression ($Ecad^{hi}$) and the other with no or low E-cadherin expression ($Ecad^{lo}$). Flow cytometry of each group revealed over 37-fold increases in the fraction of cells with dense MFN labeling from $Ecad^{hi}$ cells (5.5%) as compared to $Ecad^{lo}$ cells (0.15%) (Fig. 2g). This analysis indicates that MFN labeling of Halo-Ecad-GFP has good target-specificity.

To investigate nanoparticle labeling at single-cell and sub-cellular levels, we performed confocal fluorescence or dark-field scattering imaging of cells targeted by MFNs or MPNs, respectively. We first examined the nanoparticle labeling to Notch receptors (Fig. 3a,b, Fig. S9). A wide-field fluorescence image showed a large number of cells with Notch1 expression (mCherry) and MFN labeling (AF647) (Fig. 3a). Dark-field imaging of cells treated with MPNs identified the cells with bright scattering signals at the apical membranes (Fig. 3b). Whereas, cells incubated with non-targeting nanoparticles showed negligible signals (Fig. 3a,b)[28]. These are consistent with the flow cytometry results where both MFNs and MPNs are capable of efficient and specific labeling of Notch, a more accessible protein at the cell surface.

We then investigated E-cadherin labeling with MFNs by fluorescence imaging. Cells co-expressing Notch and E-cadherin were treated with MFNs targeting E-cadherin and imaged by confocal microscopy. Wide-field fluorescence images of cells treated with MFNs showed a substantial number of cells expressing E-cadherin with bright AF647 signals from nanoparticles (Fig. 3c, Fig. S10). In contrast, cells treated with MPNs showed very weak nanoparticle signals, indicating poor labeling (Fig. 3d). We observed negligible AF647 signals in the cells treated with non-targeting MFNs, indicating excellent target-specificity and minimum non-specific binding (Fig. 3c). To assess subcellular spatial distributions of MFNs and target proteins, we performed z-stack 3D imaging of the cells via confocal microscopy. The fluorescence signals from Halo-Ecad-GFP were distributed throughout the cytoplasm and membrane (Fig. S11). We observed significant accumulations of MFN signals at the both apical and basal membranes, indicating nanoparticle localization at the cell membranes (Fig. 3e, Fig. S11). MFN labeling to basal membrane proteins further supports its highly enhanced access of targets in crowded environments.

We aimed to demonstrate the capacity of the MFNs as mechanogenetic probes to regulate cell surface receptors in a crowded microenvironment. We labeled cells stably co-expressing SNAP-hN1-mC and Halo-Ecad-GFP receptors with MFNs via chloroalkane-Halo chemistry. Spatial and mechanical control of targeted receptors can be achieved by adjusting μ-

magnetic tweezers (μMT) modes of stimulation[29], while monitoring particle and receptor responses in 3D. Because MFNs and MPNs have an identical magnetic core (*i.e.* 13 nm $Zn_{0.4}Fe_{2.6}O_4$) coated with 2 nm SiO_2 shell (Fig. S1c), we estimated force (F) generated by a single MFN by a power law equation of $F = 0.48d_{(\mu m)}^{-4.86} + 3.06d_{(\mu m)}^{-1.43}$, where d corresponds the distance between μMT and MFNs, as described previously[28,29]. We placed μMT 5 μm above a cell's subcellular region to induce receptor clustering[29]. We monitored spatial distributions of MFNs and receptors. Initially, both MFNs and E-cadherin were uniformly distributed over the cellular edges (Fig. 4a). After the μMT application, MFNs and hence E-cadherin were spatially concentrated at the proximity of the μMT (Fig. 4a). Fluorescence increases from MFNs and E-cadherin spatial redistribution have a positive correlation (R^2=0.84, n=5) based on multiple single-cell experiments (Fig. S12a). 3D reconstruction images showed that the majority of signals from MFNs and E-cadherin were co-localized at the apical membrane (Fig. 4d, Fig. S13).

We further investigated dynamics of E-cadherin-mediated adherens junction formation in 3D space. To image F-actin, we transfected U2OS cells expressing SNAP-hN1 and Halo- Ecad-GFP with Lifeact7-mCherry. We induced E-cadherin clustering by placing the μMT above the target locations. Both MFN and E-cadherin fluorescence signals simultaneously increased and co-localized at the target subcellular locations (Fig. 4b). mCherry signals for F-actin also significantly increased and co-localized at the same locations, suggesting F-actin recruitment near the site of the E-cadherin cluster (Fig. 4b,c)[50–52]. Signal increases from E-Cadherin clustering and F-actin recruitment within same cells have a strong positive correlation (R^2=0.90, n=5) (Fig. S12b). Fluorescence signals from co-localized MFNs, E-cadherin, and F-actin all showed statistically significant 2.0-, 2.6-, and 2.8-folds increases in average intensities compared to initial values (MFN: $p<0.01$; E-cadherin: $p<0.05$; Actin: $p<0.001$) (Fig. 4e, Fig. S14). With confocal microscopy, we visualized formation of local F-actin remodeling and assembly in 3D space. An X-Z cross-section image showed the formation of thick stripe-like F-actin enrichment. In 3D space, this corresponds to a pyramidal architecture with cadherin clusters as its vertex (Fig. 4f, Fig. S15). We interpret the structure as F-actin flow towards cadherin clusters in 3D. Recent studies have revealed that cadherin-based cell adhesion is involved in contact inhibition of locomotion, a critical process for cell migration by coordinating the spatial dynamics of actin networks[53]. Thus, the MFN-based approach may be extended to investigate a variety of cellular processes, such as polarization, motility, and development, where receptor spatial heterogeneity plays a critical role in regulating downstream signaling and cellular behaviors.

In conclusion, we developed an improved mechanogenetic platform based on MFNs. We demonstrated MFN probes provided the superior labeling of surface receptors in a crowded microenvironment compared to previous MPN probes. We achieved spatiotemporal control of the membrane distribution of targeted receptors, and interrogated cellular responses to mechanogenetic perturbation using 3D confocal imaging. Note that current study did not take into account the effect of nanoscale spatial constraints of receptors (e.g. receptor oligomerization) into the nanoparticle labeling. Although we remain this for future study, small MFNs would also be useful for assessing the receptor oligomers. Finally, this study demonstrates MFNs as robust and versatile probes with the potential of mechanogenetic interrogation of a wide range of mechanosensitive cell signaling systems.

Supplementary Material

Refer to Web version on PubMed Central for supplementary material.

Acknowledgements

This work was supported by IBS-R026-D1 from IBS (J.C. and Y.J.), 1R01GM112081 and 1R01GM126542–01 from the National Institute of General Medical Science (NIGMS) and the National Institute of Health (NIH) (Y.J.), R21CA224364–01 from the National Cancer Institute (NCI) and the National Institute of Health (NIH) (Y.J.), 1R21NS103240 from the National Institute of Neurological Disorders and Stroke (NINDS) and the NIH (Y.J.), and NRF-2017M3D9A1073494 (Y.H.K.) from the National Research Foundation of Korea (KRF). M.K. is supported by a Life Science Research Foundation Shurl and Kay Curci Foundation fellowship, Burroughs Wellcome Fund, and NRF-2017R1D1A1B03035910.

References

(1). Levskaya A; Weiner OD; Lim WA; Voigt CA Nature 2009, 461 (7266), 997–1001. [PubMed: 19749742]

(2). Wu YI; Frey D; Lungu OI; Jaehrig A; Schlichting I; Kuhlman B; Hahn KM Nature 2009, 461 (7260), 104–108. [PubMed: 19693014]

(3). Toettcher JE; Voigt CA; Weiner OD; Lim WA Nature Methods 2010, 8 (1), 35–38. [PubMed: 21191370]

(4). Deisseroth K Nature Methods 2010, 8 (1), 26–29. [PubMed: 21191368]

(5). Tseng P; Judy JW; Di Carlo D Nature Methods 2012, 9, 1113. [PubMed: 23064517]

(6). Deeg J; Axmann M; Matic J; Liapis A; Depoil D; Afrose J; Curado S; Dustin ML; Spatz JP Nano Lett. 2013, 13 (11), 5619–5626. [PubMed: 24117051]

(7). Guasch J; Hoffmann M; Diemer J; Riahinezhad H; Neubauer S; Kessler H; Spatz JP Nano Lett. 2018, 18 (9), 5899–5904. [PubMed: 30088769]

(8). Matic J; Deeg J; Scheffold A; Goldstein I; Spatz JP Nano Lett. 2013, 13 (11), 5090–5097. [PubMed: 24111628]

(9). Liu Z; Liu Y; Chang Y; Seyf HR; Henry A; Mattheyses AL; Yehl K; Zhang Y; Huang Z; Salaita K Nature Methods 2015, 13 (2), 143–146. [PubMed: 26657558]

(10). Shaw A; Lundin V; Petrova E; Fordos F; Benson E; Al-Amin A; Herland A; Blokzijl A; Hogberg B; Teixeira AI Nature Methods 2014, 11 (8), 841–846. [PubMed: 24997862]

(11). Kiessling LL; Gestwicki JE; Strong LE Current opinion in chemical biology 2000, 4 (6), 696–703. [PubMed: 11102876]

(12). Dutta PK; Zhang Y; Blanchard AT; Ge C; Rushdi M; Weiss K; Zhu C; Ke Y; Salaita K Nano Lett. 2018, 18 (8), 4803–4811. [PubMed: 29911385]

(13). Albanese A; Tang PS; Chan WC W. Annu Rev Biomed Eng 2012, 14, 1–16.

(14). Pelaz B; Jaber S; de Aberasturi DJ; Wulf V; Aida T; la Fuente, de JM; Feldmann J; Gaub HE; osephson L; Kagan CR; Kotov NA; Liz-Marzán LM; Mattoussi H; Mulvaney P; Murray CB; Rogach AL; Weiss PS; Willner I; Parak WJ ACS Nano 2012, 6 (10), 8468–8483. [PubMed: 23016700]

(15). Kim BYS; Jiang W; Oreopoulos J; Yip CM; Rutka JT; Chan WC W. Nano Lett. 2008, 8 (11), 3887–3892.

(16). Medintz IL; Uyeda HT; Goldman ER; Mattoussi H Nature Mater 4, 435EP–. [PubMed: 15928695]

(17). Farlow J; Seo D; Broaders KE; Taylor MJ; Gartner ZJ; Jun Y-W Nature Methods 2013, 10 (12), 1203–1205. [PubMed: 24122039]

(18). Mannix RJ; Kumar S; Cassiola F; Montoya-Zavala M; Feinstein E; Prentiss M; Ingber DE Nat Nanotechnol 2008, 3 (1), 36–40. [PubMed: 18654448]

(19). Bonnemay L; Hostachy S; Hoffmann C; Gautier J; Gueroui Z Nano Lett. 2013, 13 (11), 5147–5152. [PubMed: 24111679]

(20). Etoc F; Vicario C; Lisse D; Siaugue J-M; Piehler J; Coppey M; Dahan M Nano Lett. 2015, 15 (5), 3487–3494. [PubMed: 25895433]

(21). Etoc F; Lisse D; Bellaiche Y; Piehler J; Coppey M; Dahan M Nat Nanotechnol 2013, 8 (3), 193–198. [PubMed: 23455985]

(22). Singha S; Shao K; Yang Y; Clemente-Casares X; Solé P; Clemente A; Blanco J; Dai Q; Song F; Liu SW; Yamanouchi J; Umeshappa CS; Nanjundappa RH; Detampel P; Amrein M; Fandos C; Tanguay R; Newbigging S; Serra P; Khadra A; Chan WCW; Santamaria P Nat Nanotechnol 2017, 12 (7), 701–. [PubMed: 28436959]

(23). Hoffmann C; Mazari E; Lallet S; Le Borgne R; Marchi V; Gosse C; Gueroui Z Nat Nanotechnol 2013, 8 (3), 199–205. [PubMed: 23334169]

(24). Lee J-H; Kim ES; Cho MH; Son M; Yeon S-I; Shin J-S; Cheon J Angewandte Chemie International Edition 2010, 49 (33), 5698–5702. [PubMed: 20607781]

(25). Cho MH; Lee EJ; Son M; Lee J-H; Yoo D; Kim J-W; Park SW; Shin J-S; Cheon J Nature Mater 2012, 11 (12), 1038–1043. [PubMed: 23042417]

(26). Chen R; Canales A; Anikeeva P Nature Reviews Materials 2017, 2, 16093.

(27). Colombo M; Carregal-Romero S; Casula MF; Gutiérrez L; Morales MP; Böhm IB; Heverhagen JT; Prosperi D; Parak WJ Chem. Soc. Rev 2012, 41 (11), 4306–4334. [PubMed: 22481569]

(28). Seo D; Southard KM; Kim J-W; Lee HJ; Farlow J; Lee J-U; Litt DB; Haas T; Alivisatos AP; Cheon J; Gartner ZJ; Jun Y-W Cell 2016, 165 (6), 1507–1518. [PubMed: 27180907]

(29). Kim J-W; Seo D; Lee J-U; Southard KM; Lim Y; Kim D; Gartner ZJ; Jun Y-W; Cheon J Nat Protoc 2017, 12 (9), 1871–1889. [PubMed: 28817122]

(30). Haltiwanger RS; Lowe JB Annu. Rev. Biochem 2004, 73 (1), 491–537. [PubMed: 15189151]

(31). Paszek MJ; DuFort CC; Rossier O; Bainer R; Mouw JK; Godula K; Hudak JE; Lakins JN; Wijekoon AC; Cassereau L; Rubashkin MG; Magbanua MJ; Thorn KS; Davidson MW; Rugo HS; Park JW; Hammer DA; Giannone G; Bertozzi CR; Weaver VM Nature 2014, 511, 319. [PubMed: 25030168]

(32). Atukorale PU; Yang Y-S; Bekdemir A; Carney RP; Silva PJ; Watson N; Stellacci F; Irvine DJ Nanoscale 2015, 7 (26), 11420–11432. [PubMed: 26077112]

(33). Boggon TJ Science 2002, 296 (5571), 1308–1313. [PubMed: 11964443]

(34). Gordon WR; Vardar-Ulu D; Histen G; Sanchez-Irizarry C; Aster JC; Blacklow SC Nat Struct Mol Biol 2007, 14 (4), 295–300. [PubMed: 17401372]

(35). Susumu K; Uyeda HT; Medintz IL; Pons T; Delehanty JB; Mattoussi HJ Am. Chem. Soc 2007, 129 (45), 13987–13996.

(36). Palui G; Aldeek F; Wang W; Mattoussi H Chem. Soc. Rev 2015, 44 (1), 193–227. [PubMed: 25029116]

(37). Zanchet D; Micheel CM; Parak WJ; Gerion D; Alivisatos AP Nano Lett. 2001, 1 (1), 32–35.

(38). Jewett JC; Sletten EM; Bertozzi CR J. Am. Chem. Soc 2010, 132 (11), 3688–3690. [PubMed: 20187640]

(39). Yi G; Son J; Yoo J; Park C; Koo H Biomater Res 2018, 22 (1), 903.

(40). Claridge SA; Liang HW; Basu SR; Fréchet JMJ; Alivisatos AP Nano Lett. 2008, 8 (4), 1202–1206. [PubMed: 18331002]

(41). Sonnichsen C; Reinhard BM; Liphardt J; Alivisatos AP Nat. Biotechnol 2005, 23 (6), 741–745. [PubMed: 15908940]

(42). Parak WJ; Pellegrino T; Micheel CM; Gerion D; Williams SC; Alivisatos AP Nano Lett. 2003, 3 (1), 33–36.

(43). Claridge SA; Goh SL; Fréchet JMJ; Williams SC; Micheel CM; Alivisatos AP Chemistry of Materials 2005, 17 (7), 1628–1635.

(44). Yi DK; Selvan ST; Lee SS; Papaefthymiou GC; Kundaliya D; Ying JY J. Am. Chem. Soc 2005, 127 (14), 4990–4991. [PubMed: 15810812]

(45). Chen O; Riedemann L; Etoc F; Herrmann H; Coppey M; Barch M; Farrar CT; Zhao J; Bruns OT; Wei H; Guo P; Cui J; Jensen R; Chen Y; Harris DK; Cordero JM; Wang Z; Jasanoff A; Fukumura D; Reimer R; Dahan M; Jain RK; Bawendi MG Nature Communications 2014, 5, 5093.

(46). Pittet MJ; Swirski FK; Reynolds F; Josephson L; Weissleder R Nat Protoc 2006, 1, 73. [PubMed: 17406214]

(47). Morsut L; Roybal KT; Xiong X; Gordley RM; Coyle SM; Thomson M; Lim WA Cell 2016, 164 (4), 780–791. [PubMed: 26830878]

(48). Mumm JS; Schroeter EH; Saxena MT; Griesemer A; Tian X; Pan DJ; Ray WJ; Kopan R Molecular Cell 2000, 5 (2), 197–206. [PubMed: 10882062]

(49). Gordon WR; Vardar-Ulu D; Histen G; Sanchez-Irizarry C; Aster JC; Blacklow SC Nat Struct Mol Biol 2007, 14 (4), 295–300. [PubMed: 17401372]

(50). Lecuit T; Yap AS Nature Cell Biology 2015, 17, 533. [PubMed: 25925582]

(51). Dejana E; Orsenigo F; Lampugnani MG Journal of Cell Science 2008, 121 (13), 2115–2122. [PubMed: 18565824]

(52). Engl W; Arasi B; Yap LL; Thiery JP; Viasnoff V Nature Cell Biology 2014, 16 (6), 584–591.

(53). Davis JR; Luchici A; Mosis F; Thackery J; Salazar JA; Mao Y; Dunn GA; Betz T; Miodownik M; Stramer BM Cell 2015, 161 (2), 361–373. [PubMed: 25799385]

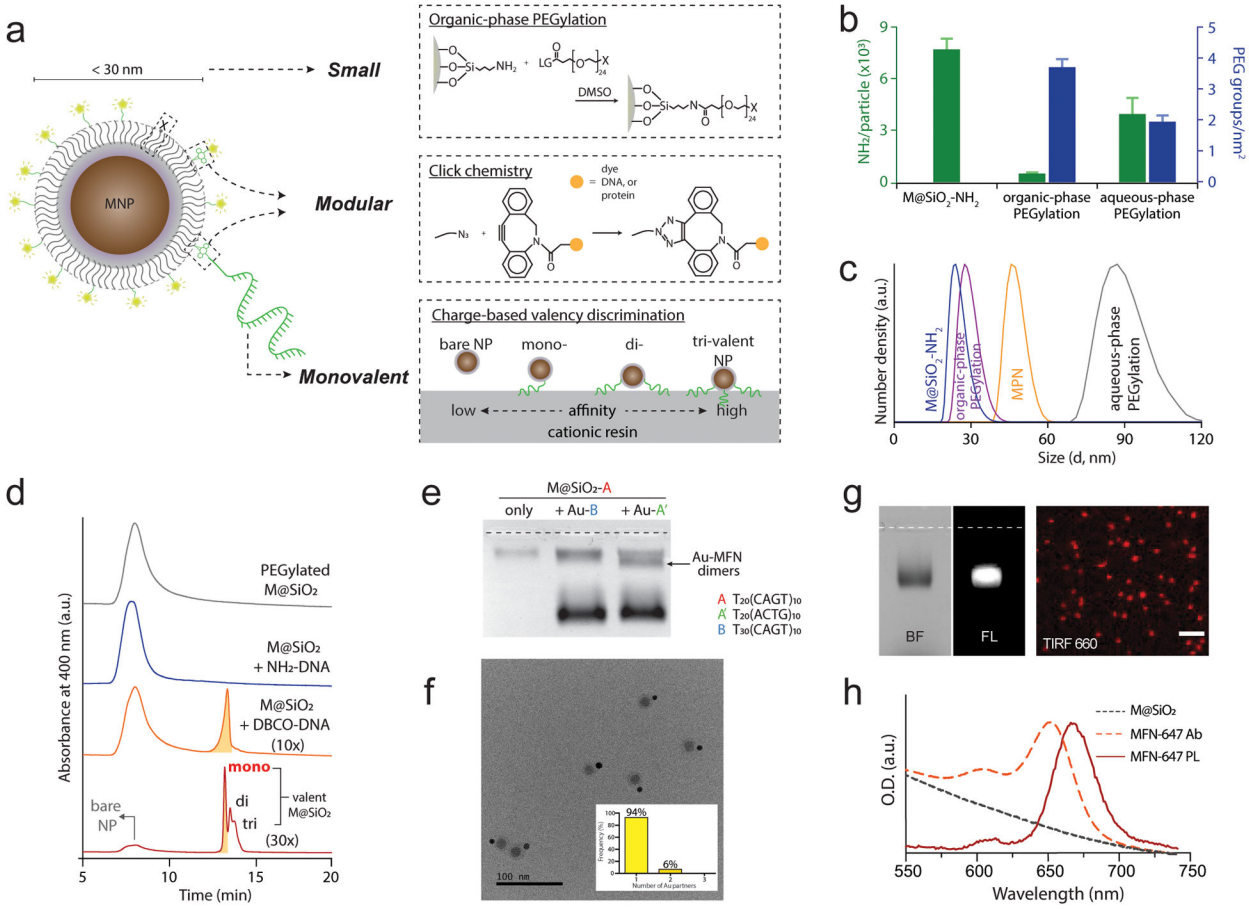

Figure 1. Design and synthesis of small, clickable, and monovalent magnetofluorescent nanoparticles (MFNs).

(a) A schematic description of MFN synthesis via organic-phase PEGylation, click chemistry, and the charge-based valency discrimination principle. (b) Amine quantification of $M@SiO_2$ nanoparticles. The number of NH_2 per nanoparticle (green) and the density of PEG_{24} coverage on nanoparticles (blue) before PEGylation, after organic-phase PEGylation, and after aqueous-phase PEGylation (n=3). (c) Dynamic light scattering (DLS) spectra of before and after the organic-phase PEGylation of $M@SiO_2$. For comparisons, DLS spectra of MPNs and PEGylated $M@SiO_2$ via the aqueous-phase synthesis are also shown. (d) Elution profiles of AE-HPLC for unreacted $M@SiO_2$ (grey), $M@SiO_2$ reacted with NH_2-modified DNA (blue), MFNs conjugated with 10-fold (orange) or 30-fold (red) molar excess of DBCO-modified DNA. The area highlighted with orange represents monovalent species. (e) Agarose gel electrophoresis of monovalent $M@SiO_2$ nanoparticles hybridized with 10 nm Au nanoparticles conjugated with DNA bearing complementary sequences. Lane 1: $M@SiO_2$ only. Lane 2: $M@SiO_2$ + Au with non-complementary DNA. Lane 3: $M@SiO_2$ + Au with complementary DNA. (f) A representative TEM image of $M@SiO_2$-Au heterodimers purified from gel electrophoresis. Insert: Approximately 94% of detected species were $M@SiO_2$-Au heterodimers. (g) Left: A gel electrophoresis image of MFN-AF647 confirms fluorescent properties. Right: a TIRF image of MFN-AF647. Scale bar = 1 μm. (h) Absorption (Ab) and photoluminescence (PL) spectra of MFN-AF647. An

absorption spectrum of the PEGylated M@SiO_2 without dye conjugation shown as a control (black dashed line).

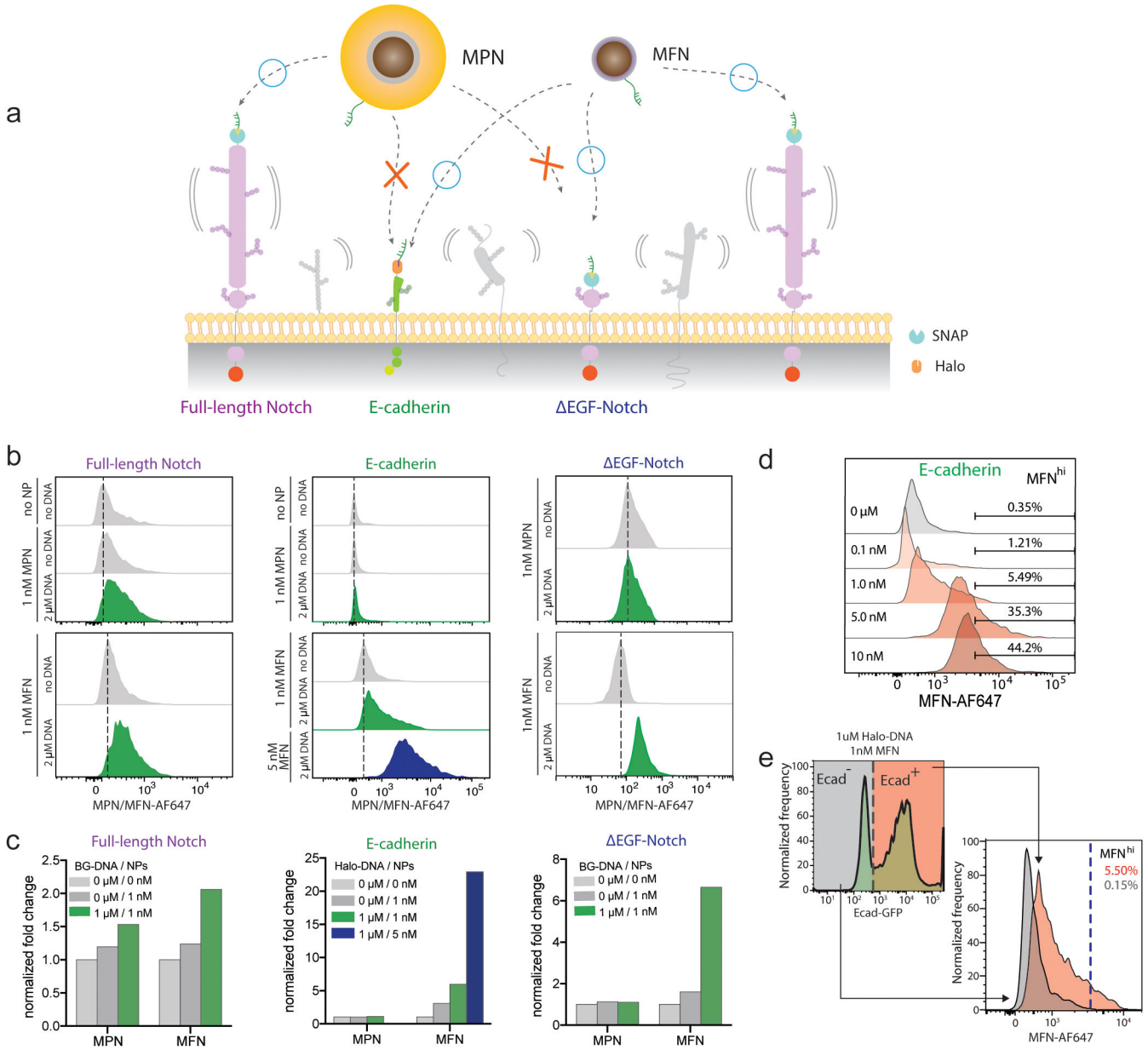

Figure 2. Flow cytometry analysis (FCA) to evaluate MFN labeling to target receptors in a crowded live cell microenvironment.

(a) Schematic illustration of nanoparticle labeling to cell surface receptors. MFNs have a smaller hydrodynamic size, thus enabling more efficient labeling of Notch, ΔEGF-Notch, and E-cadherin than MPNs. (b) Left: FCA of Notch and E-cadherin co-expressing treated with the indicated conditions for nanoparticle labeling of Notch. Center: FCA of Notch and E-cadherin co-expressing cells treated with the indicated conditions for nanoparticle labeling of E-cadherin. Right: FCA of ΔEGF-Notch expressing cells treated with the indicated conditions for nanoparticle labeling of ΔEGF-Notch. (c) Geometric means of AF647 intensity for nanoparticle signals from cells treated with the indicated labeling conditions. Each bar graph is for targeting of the indicated receptors. (d) FCA of the cells incubated with varying concentrations of MFNs for labeling of E-cadherin. (e) FCA showing target

specificity of MFN labeling of E-cadherin. Left: E-cadherin signals (GFP) of the cells. Cells were grouped into two subsets, $Ecad^{hi}$ and $Ecad^{lo}$ cells. Right: FCA in MFN-AF647 signals from the $Ecad^{hi}$ (red) and $Ecad^{lo}$ subsets (grey).

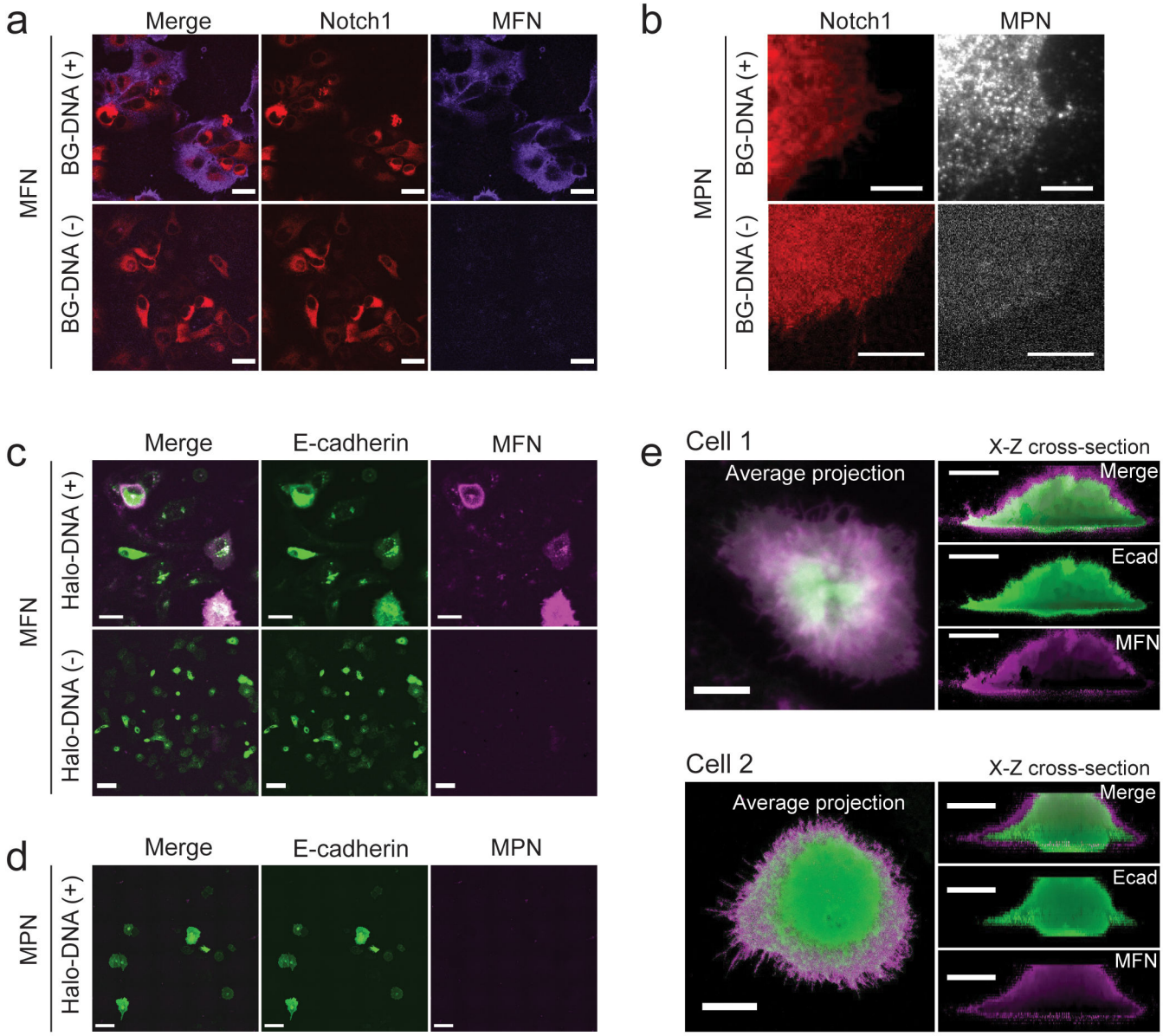

Figure 3. Comparison in receptor accessibility of MFNs with MPN via 3D confocal fluorescence imaging.

(a) Notch expression (red) and MFN labeling (magenta) observed via wide-field microscopy. A representative image of SNAP-hN1-mC expressing U2OS cells treated with BG-DNA and MFNs (top), and negative control cells incubated without BG-DNA (bottom). Scale bar = 100 μm. (b) Efficient MPN labeling of Notch (red) observed using dark-field (DF) reflective microscopy. The DF images of cells incubated with BG-DNA and MPNs show dense nanoparticle labeling (top), while DF images of cells incubated with only MPNs but no BG-DNA show minimal labeling (bottom). Scale bar = 3 μm. (c) E-cadherin expression (green) and MFN labeling (magenta) observed via wide-field epifluorescence microscopy. A representative image of SNAP-hN1-mC and Halo-Ecad-GFP co-expressing cells incubated with Halo-DNA and MFNs shows dense MFN labeling (top, scale bar=100 μm). The image

of cells treated with MFNs but no Halo-DNA shows minimal labeling (bottom, scale bar = 30 μm). (d) Limited labeling of E-cadherin by MPNs. A representative wide-field image of cells incubated with Halo-DNA and MPNs exhibit high E-cadherin expression (green) but negligible MPN labeling (magenta). Scale bar = 100 μm. (e) Confocal microscopy images of two cells labeled with dense MFNs. Left: average projection of Z-stack images. Scale bar = 20 μm. Right: a X-Z cross-section of the 3D reconstruction based on maximum intensity. Scale bar = 20 μm.

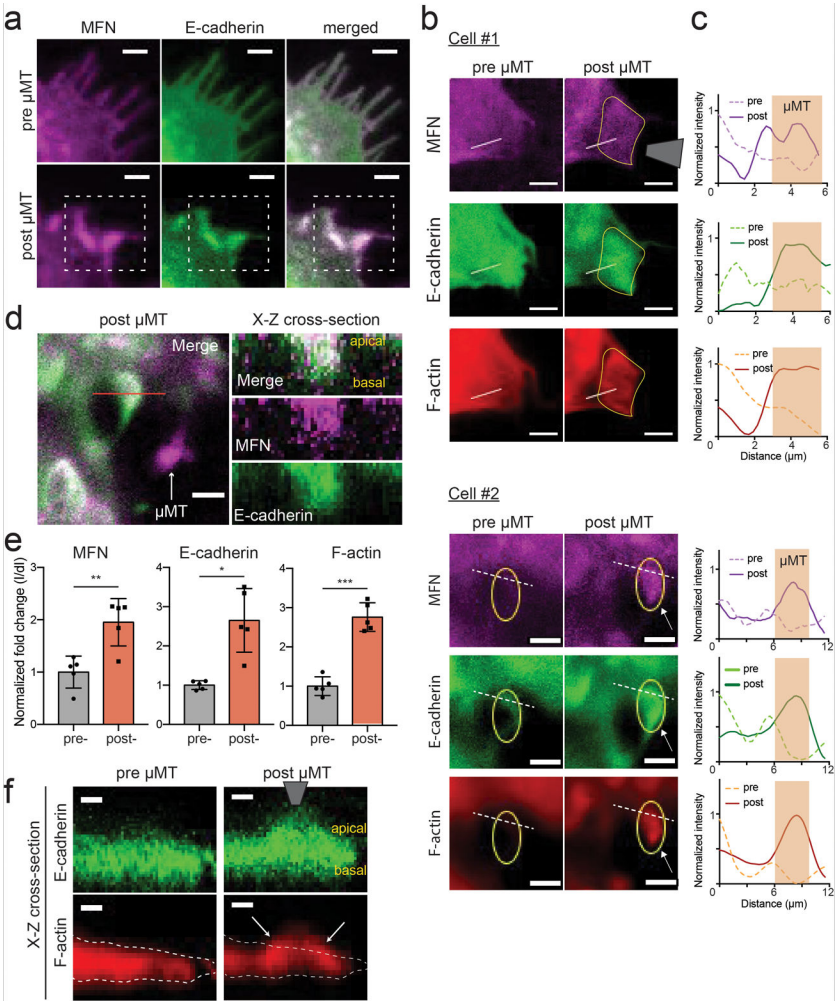

Figure 4. Mechanogenetic interrogation of E-cadherin mediated adherens junction formation in 3D.

(a) A confocal image of a representative cell to monitor localization of MFNs (magenta) and E-cadherin (green; E-cad) before and after μMT application. The μMT was placed at 5 μm above the targeted location (white dashed rectangle). Scale bar = 5 μm. (b) confocal images depicting the spatial distribution of MFNs (magenta, top), E-cad (green, middle), and F-actin (red, bottom) before (left) and 10 min. after (right) the μMT application. The affected regions are highlighted with yellow solid shapes. Scale bar = 5 μm. (c) Line scan profiles of MFNs, E-cadherin, and F-actin before (dashed lines) and after (solid lines) μMT application for the white lines shown in (b). The line segments within the targeted locations of mechanogenetic regulation of E-cadherin were indicated with brown shade. (d) Left: average projection of cell #2 (Fig. 4b) after μMT application. The white arrow indicates a probe tip coated with MFNs prior to the experiment. Right: An X-Z cross-section image of the same cell through the solid red line. Scale bar = 5 μm. (e) Normalized fluorescence intensities for MFNs, E-cad, and F-actin before and after mechanogenetic perturbation (n=5). * $p < 0.05$, ** $p < 0.01$, *** $p < 0.001$. (f) The X-Z cross-section of the cell #1, panel (b). White dashed

lines show the cell boundary before μMT application. White arrows indicate the F-actin enrichment. Scale bar = 2 μm.